ACS central science

Research Article

Cite This: ACS Cent. Sci. 2018, 4, 1244−1252

http://pubs.acs.org/journal/acscii

# Iridium−Tungsten Alloy Nanodendrites as pH-Universal Water-Splitting Electrocatalysts

Fan Lv,[†] Jianrui Feng,[†] Kai Wang,[†] Zhipeng Dou,[§] Weiyu Zhang,[†] Jinhui Zhou,[†] Chao Yang,[†] Mingchuan Luo,[†] Yong Yang,[†] Yingjie Li,[†] Peng Gao,[§] and Shaojun Guo*[,†,‡,∥,⊥]

[†]Department of Material Science and Engineering, College of Engineering, Peking University, Beijing 100871, P. R. China

[‡]BIC-ESAT, College of Engineering, Peking University, Beijing 100871, P. R. China

[§]Electron Microscopy Laboratory, and International Center for Quantum Materials, School of Physics, Peking University, Beijing 100871, P. R. China

[∥]Department of Energy and Resources Engineering, College of Engineering, Peking University, Beijing 100871, P. R. China

[⊥]Beijing Key Laboratory for Magnetoeletric Materials and Devices (BKL-MEMD), Peking University, Beijing 100871, P. R. China

Supporting Information

**ABSTRACT:** The development of highly efficient and durable electrocatalysts for high-performance overall water-splitting devices is crucial for clean energy conversion. However, the existing electrocatalysts still suffer from low catalytic efficiency, and need a large overpotential to drive the overall water-splitting reactions. Herein, we report an iridium−tungsten alloy with nanodendritic structure (IrW ND) as a new class of high-performance and pH-universal bifunctional electrocatalysts for hydrogen and oxygen evolution catalysis. The IrW ND catalyst presents a hydrogen generation rate ∼2 times higher than that of the commercial Pt/C catalyst in both acid and alkaline media, which is among the most active hydrogen evolution reaction (HER) catalysts yet reported. The density functional theory (DFT) calculations reveal that the high HER intrinsic catalytic activity results from the suitable hydrogen and hydroxyl binding energies, which can accelerate the rate-determining step of the HER in acid and alkaline media. Moreover, the IrW NDs show superb oxygen evolution reaction (OER) activity and much improved stability over Ir. The theoretical calculation demonstrates that alloying Ir metal with W can stabilize the formed active iridium oxide during the OER process and lower the binding energy of reaction intermediates, thus improving the Ir corrosion resistance and OER kinetics. Furthermore, the overall water-splitting devices driven by IrW NDs can work in a wide pH range and achieve a current density of 10 mA cm$^{-2}$ in acid electrolyte at a low potential of 1.48 V.

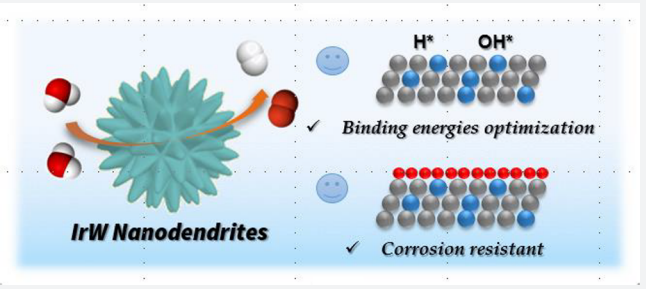


## INTRODUCTION

Electrocatalytic water splitting is one of the most promising technologies for the conversion of electricity from renewable sources such as solar, wind, and water, to mitigate their uneven distribution in time and space.[1,2] As two half-reactions of a water-splitting device, the hydrogen evolution reaction (HER) and oxygen evolution reaction (OER), involving multiple-proton-coupled electron transfer, require a large overpotential due to their sluggish kinetics, which seriously affect the energy efficiency of the whole device.[3,4] Therefore, developing highly efficient bifunctional catalysts enabled for both the HER and OER is of great significance. For current HER catalysts, Pt usually represents the best activity for the HER because Pt sits on the vertex of the HER volcano plot. Ir, usually considered as an OER catalyst, is also located near the vertex of the HER volcano plot.[5,6] Nevertheless, to date, it is still a great challenge to design Ir-based metal catalysts, which can show a comparable intrinsic HER activity to Pt.[7,8] Meanwhile, understanding the HER reaction process and rate-determining step on Ir-based materials is still an open question, particularly in different pH conditions.[6,9] On the whole, the descriptor of the HER can be attributed to the hydrogen binding energy in the acid, whereas in the base, hydroxyl binding energy on the catalyst makes a difference.[10−12] Synergic optimization of these two binding energies on Ir may be an effective strategy to achieve an HER activity better than Pt in a wide pH range, however, designing Ir-based catalysts with the optimized hydrogen binding energy and hydroxyl binding energy at all pH values is still a grand challenge.

As for the OER, Ir-based materials are known as the state-of-the-art electrocatalysts with the acceptable knowledge that the active ingredient is the oxides ($IrO_x$).[13,14] Great efforts have been devoted to comprehending the property−function relationship on their activity and stability.[15−18] To date, the volcano relationship of activity and oxygen intermediate binding

Received: July 4, 2018
Published: August 29, 2018






DOI: 10.1021/acscentsci.8b00426
ACS Cent. Sci. 2018, 4, 1244−1252

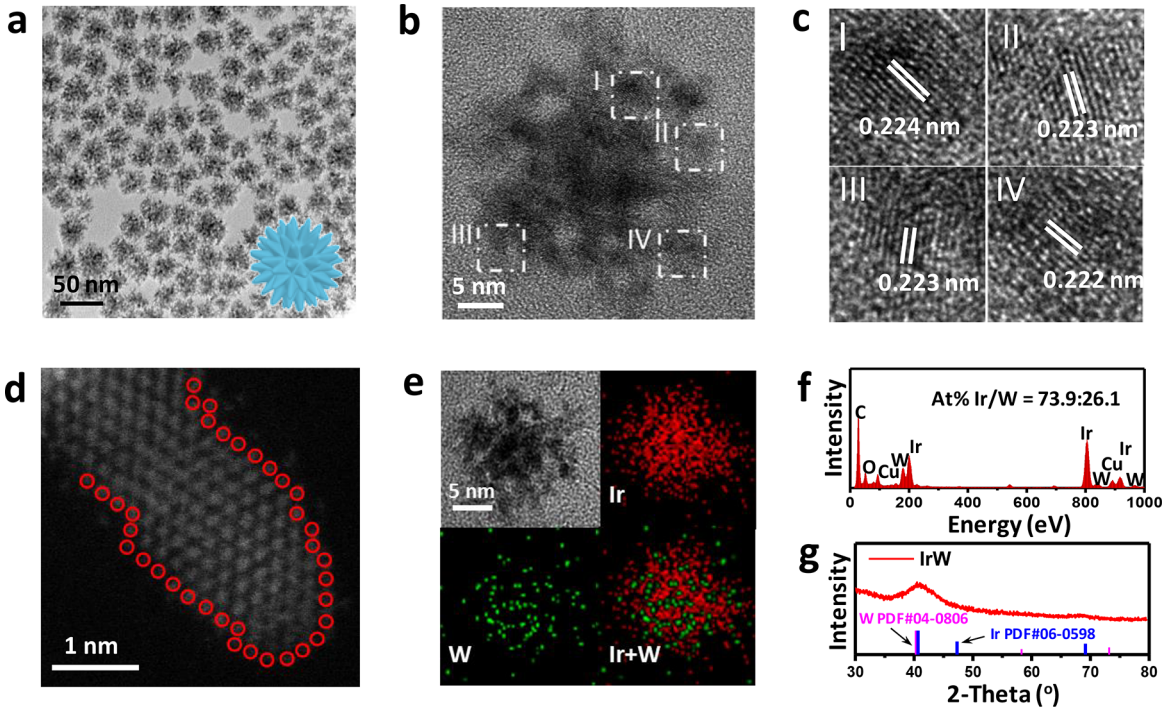


**Figure 1.** Morphology and phase characterization of IrW nanodendrites. (a) TEM, (b, c) HRTEM, (d) HAADF-STEM, (e) EDS-mapping images, (f) XRD pattern, and (g) EDS spectrum of IrW NDs.

energy has been well-employed to design the active OER catalyst.[5,19] Binding of the oxygen intermediates on $IrO_2$ that is too strong limits the further improvement of its activity.[20] Meanwhile, the corrosion of Ir is another severe issue in the long-stability test, and unfortunately highly active $IrO_x$ always suffers from the drastic erosion.[21,22] Hence, balancing both of these two factors of Ir(IV) is a challenging mission for the community.[23] Recent advances on Ir-based catalysts indicate that their OER stability and activity do not strictly follow the reciprocal relation.[15,20] Particularly, the electrochemical pre-oxidized Ir nanoparticles are capable of maintaining better stability and activity compared with undisposed Ir nanoparticles and crystalline $IrO_2$ because fewer unstable Ir species are formed under OER conditions.[20] However, adsorption energy regulation and corrosion inhibition have never been achieved together in Ir-based electrocatalysts.

Herein, we report a new method for making iridium−tungsten alloy nanodendritic structures (IrW NDs) with porous structure as a class of highly efficient electrocatalysts for both the HER and OER at all pH conditions. The IrW ND catalyst presents ∼2 times higher HER turnover frequency (TOF) per Ir site than the commercial Pt/C catalyst, which is the best Ir-based HER catalyst. The density functional theory (DFT) calculations reveal that the activation energies of the HER rate-determining step in acid and alkaline media are optimized on our IrW alloy, thus boosting the HER catalytic activity. Meanwhile, the IrW NDs also achieve 3 times higher current density than the Ir/C at the 1.53 V versus reversible hydrogen electrode (RHE) and superior stability after the accelerated degradation test (ADT) of 3000 cycles. The theoretical calculation demonstrates that W can stabilize the formed active iridium oxide during the OER process, and the W-doped $IrO_2$ possesses lower binding energy of oxygen intermediates than $IrO_2$, which hinders the dissolution of Ir and accelerates its OER kinetics. Furthermore, the superb bifunctional HER and OER performance of IrW NDs makes them exhibit high performance in a water electrolyzer at all pH values.

## RESULTS AND DISCUSSION

**Synthesis and Characterization of IrW NDs.** The IrW NDs were synthesized by a colloidal-chemical approach, using iridium(III) chloride hydrate ($IrCl_3{\cdot}xH_2O$) and tungsten carbonyl ($W(CO)_6$) as the metal precursors, oleylamine as solvent, cetyltrimethylammonium chloride (CTAC) as surfactant, and glucose as a reducing agent (details in the Methods section). Figure 1a and Figure S1 show the typical transmission electron microscopy (TEM) image of the prepared IrW NDs. They exhibit a highly porous nanostructure with the size of 25 ± 2 nm, and consist of multiple tiny branchlike and overlapped nanoparticles (Figure 1b). The high-resolution TEM (HRTEM) and corresponding fast Fourier transformation (FFT) patterns of the IrW NDs indicate that they employ the *fcc* phase (Figure S2). Lattice spacings measured from different branches in the high-magnification HRTEM of one IrW ND (Figure 1c and Figure S2) are averaged at 0.223 and 0.192 nm, corresponding to the (111) and (002) planes of IrW alloy. The aberration-corrected high-angle annular dark-field scanning (HAADF-STEM) was performed to further reveal the atomic-scale surface structure of individual branchlike nanoparticles. The enlarged HAADF-STEM image of IrW NDs in Figure S3 indicates that the surface contains atomic steps and kinks (Figure 1d). The element distribution of Ir and W at the NDs was characterized by TEM energy-dispersive X-ray spectroscopy (EDS) mapping (Figure 1e). Ir (red) and W (green) elements are homogeneously distributed through whole nanodendrites, while the atomic ratio of these two elements is determined to be about 3:1 (Figure 1f), in agreement with the inductively coupled plasma atomic emission spectroscopy (ICP-AES) result. In the X-ray diffraction pattern of IrW NDs (Figure 1g), there is only one widened peak at around 40.5°



DOI: 10.1021/acscentsci.8b00426
ACS Cent. Sci. 2018, 4, 1244−1252

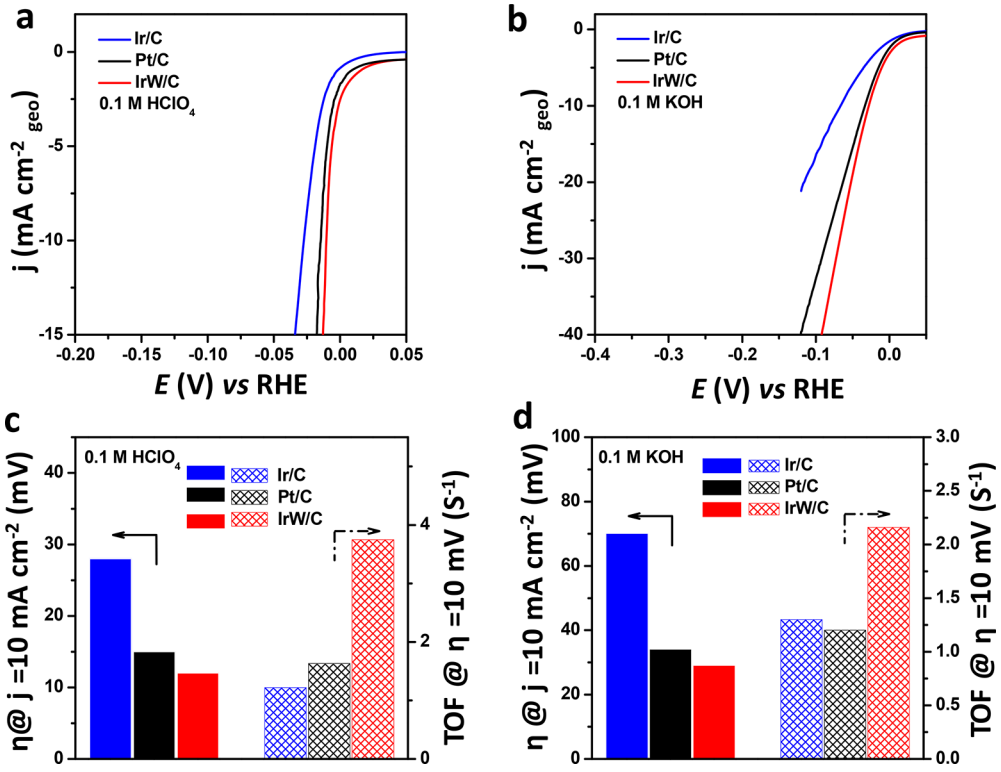


**Figure 2.** HER performance of IrW NDs in acid and alkaline electrolytes. (a, b) HER polarization curves of IrW/C, Ir/C, and Pt/C with 95% *iR*-compensation in 0.1 M $HClO_4$ and 0.1 M KOH at the scan rate of 5 mV $s^{-1}$. (c, d) Overpotentials at 10 mA $cm^{-2}$ (left) and TOFs normalized by the ECSA of IrW/C, Ir/C, and Pt/C in 0.1 M $HClO_4$ and 0.1 M KOH at an overpotential of 10 mV (right).

due to the small size of the branchlike nanoparticles, consistent with the TEM results.

The present method can be used to make IrW alloy NDs with different diameters from 10 to 50 nm by changing the amount of glucose and keeping other parameters consistent (Figure S4). In addition, only the flowerlike iridium nanostructure with relative larger particle units was obtained in the absence of $W(CO)_6$ (Figure S5), indicating that the carbon monoxide in situ decomposed from the $W(CO)_6$ in the synthetic process, which might accelerate the nucleation process of IrW alloy. Therefore, the $W(CO)_6$ not only served as the W precursor, but also played an important role in the nucleation of Ir to small nanoparticles, and then aggregating to nanodendrites.

**HER Performance of IrW NDs in Acid and Alkaline Electrolytes.** The HER catalytic properties of carbon-supported IrW NDs (IrW/C) with a clean surface were evaluated, and compared with the Ir/C and Pt/C catalysts in acid and alkaline conditions. We found that, in both acid and alkaline electrolytes, the HER performances of different catalysts follow IrW/C > Pt/C > Ir/C (Figure 2a,b). In 0.1 M $HClO_4$ solution, the overpotential of IrW/C at 10 mA $cm^{-2}$ is 12 mV (left part of Figure 2c), lower than those of Pt/C (15 mV) and Ir/C (28 mV). In 0.1 M KOH solution, the IrW/C still shows the lowest overpotential of 29 mV at 10 mA $cm^{-2}$ (left part of Figure 2d), in all the investigated catalysts (Pt/C, 34 mV; and Ir/C, 70 mV). For an elimination of the different contributions derived from diverse particle sizes and the surface structure of catalysts to the HER performance, the electrochemically active surface areas (ECSAs) of Pt/C, Ir/C, and IrW/C were measured by calculating the underpotentially deposited ($H_{upd}$) area from the cyclic voltammetry curves (Figure S6). On the basis of the ECSA and current density obtained from the polarization curves, we calculated the TOF values of different catalysts (Figure S7). At the overpotential of 10 mV, the TOF of IrW/C reaches 3.75 $s^{-1}$ in $HClO_4$ and 2.16 $s^{-1}$ in KOH, 2.3 and 1.8 times higher than those of Pt/C, and 3.0 and 1.7 times higher than those of Ir/C, respectively (right part of Figure 2c). Therefore, the HER intrinsic activity of Ir is much enhanced by alloying with W, and the HER performance of IrW is the best compared to the previous HER catalysts (Tables S1 and S2).

For a further evaluation the durability of the IrW/C catalyst, an ADT was performed at the scan rate of 20 mV $s^{-1}$. The polarization curves of the IrW/C catalyst before and after 1000 cycles overlap in both acid and base electrolytes (Figure S8). TEM images of IrW/C after the durability test also show that IrW NDs still possess a porous structure and distribute uniformly on the carbon (Figure S9), indicating its robust structure.

**HER-Enhancing Mechanism of IrW NDs.** Generally, two HER mechanisms, Volmer–Tafel and Volmer–Heyrovsky reactions, have been widely used to describe the intermediate steps, involving the conversion of $H_2O/H^+$ to $H_2$.[12] Meanwhile, these two mechanisms can be distinguished by the value of Tafel slope because of their different kinetics on the metal.[24] According to the tested values of Tafel slope in Ir/C, Pt/C, and IrW/C catalysts (Figure S10), the mechanism more likely proceeds through the Volmer–Tafel reaction in 0.1 M $HClO_4$, but follows the Volmer–Heyrovsky process in 0.1 M KOH. Furthermore, since the reacting species are different in acid ($H^+$) and alkaline ($H_2O/OH^-$) media, the Volmer and Heyrovsky steps also display different reactions in acid and base solution. On the basis of the different mechanism of the HER in acidic media and alkaline media (Figure 3a), we employed first-principles calculations based on DFT methods



DOI: 10.1021/acscentsci.8b00426
ACS Cent. Sci. 2018, 4, 1244–1252

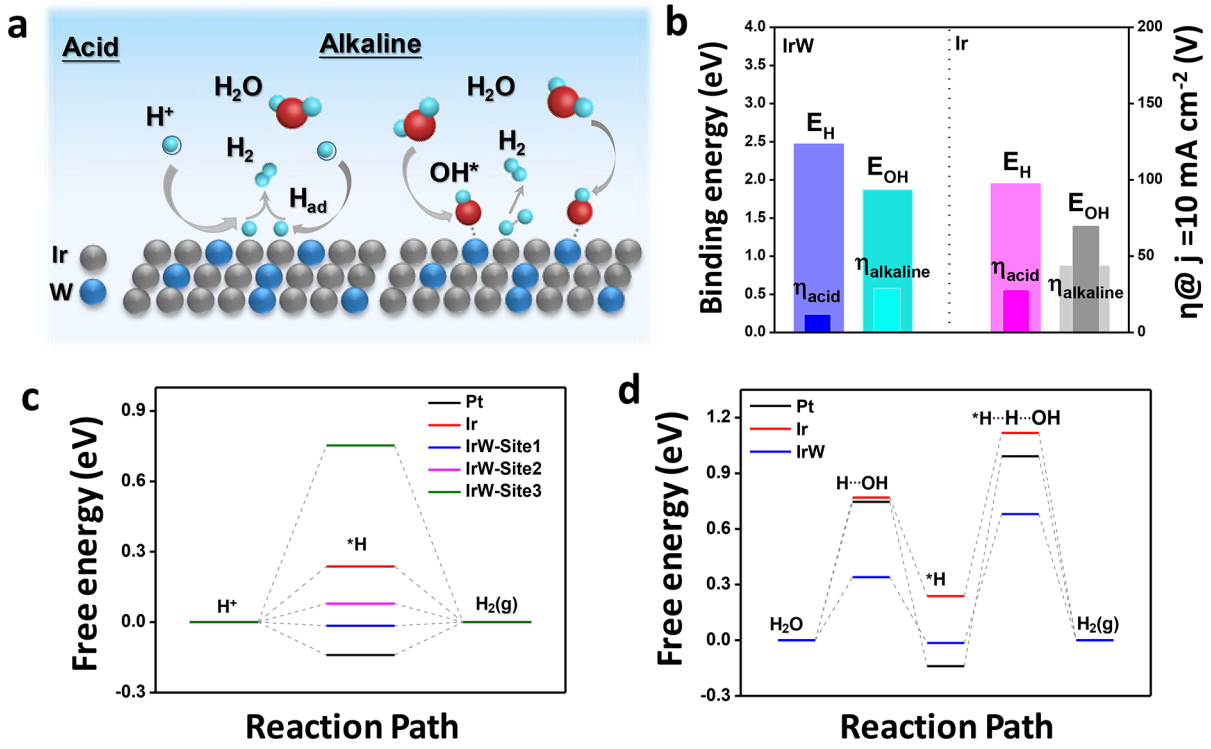


**Figure 3.** HER mechanisms of IrW NDs in acid and alkaline electrolytes. (a) Schematic illustration of the HER mechanism on IrW NDs in acid and alkaline media. (b) Trends in HER activity with varying binding energies of H and OH. (c) Free energy diagram of the HER over Pt, Ir, and IrW in acid media. (d) Free energy diagram along the reaction of the Volmer–Heyrovsky mechanism in alkaline media.

to obtain the free energy diagrams. For deep insights into the superior HER performance of IrW, the binding energies of H ($E_H$) and OH ($E_{OH}$) on different catalysts have been first calculated. The $E_H$ and $E_{OH}$ on IrW are both stronger than those of Ir, which are associated with lower overpotentials in both acidic and alkaline electrolytes (Figure 3b). In acid media, the free energy diagram based on the Volmer–Tafel mechanism is calculated as in Figure 3c, where Pt and Ir are taken as references. Different adsorption sites of H were taken into consideration (Figure S11); we found that H could generate stable adsorption on the top site of Ir, the top site of W, and the hollow site surrounded by two Ir atoms and one W atom. The most favorable site for H is the top site of Ir, corresponding to the site 1 of IrW, whose binding strength is stronger than Ir but weaker than Pt. The moderate binding strength (Sabatier principle) makes IrW the best catalyst among Ir and Pt (adsorption structures are shown in Figure S12), in accordance with electrochemical polarization curves. In alkaline solution, the HER process can be divided into Volmer and Heyrovsky stages as mentioned before, in which the dissociation of water is pivotal. Figure 3d shows the free energy diagram of the HER in alkaline solutions. First, water dissociation on the surface of the catalyst on two different positions in the Volmer reaction was simulated so that in one case the dissociated OH was bonded with W (Figure S13) and in another case bonded with Ir (Figure S14). Their barriers are, respectively, 0.34 and 0.61 eV, lower than those of Pt (0.74 eV) and Ir (0.76 eV). This shows that the key factor in enhancing HER performance in alkaline media is the active surface W with stronger binding energy for OH, rather than a single Ir activity site. Furthermore, at the Heyrovsky stage (Figure S15), the barriers for Pt, Ir, and IrW are 1.13, 0.88, and 0.67 eV, respectively. The relatively lower barrier of IrW can also be attributed to the strong affinity of the W active site to OH. In all, the rate-determining step is the Heyrovsky stage, and the order of DFT-calculated activity is as follows: IrW > Ir > Pt, being consistent with experimentally observed TOFs. To summarize, we demonstrate that the acidic HER activity is promoted by stronger adsorption of H on Ir active sites of IrW, while the alkaline HER is facilitated by a higher affinity to OH of surface W in IrW in accelerating the water dissociation process.

**OER Performance and Enhancing Mechanism of IrW NDs.** The IrW/C, Ir/C, and Pt/C catalysts were also studied for the OER performance. It is worth noting that, before the electrochemical activity test, the IrW/C and Ir/C were preoxidized through potential cycles between 0.05 and 1.5 V versus RHE several times until the stable cyclic voltammetry curves appeared, in which the peaks of H absorption/desorption vanished, and the peaks assigned to the redox of Ir(III)/Ir(IV) emerged (Figure S16). The polarization curves of the catalysts reveal that the IrW/C shows superior OER activity relative to Ir/C and Pt/C in 0.1 M $HClO_4$ (Figure 4a). The IrW/C catalyst shows a sharp onset potential at ~1.45 V versus RHE, better than the Ir/C (1.48 V) and Pt/C (1.62 V). The corresponding Tafel slope of 56.6 mV $dec^{-1}$ is the lowest among these three catalysts (inset of Figure 4a). At the overpotential of 300 mV, the IrW/C catalyst can achieve the current density of 8.1 mA $cm^{-2}$, 3.2 and 35.0 times higher than those of Ir/C and Pt/C catalysts (left part of Figure 4b). Moreover, for a determination of the alloying effort of W element on the OER intrinsic activity of Ir, the TOF values of different catalysts were calculated (Figure S17). The IrW/C catalyst exhibits a very high TOF of 1.49 $s^{-1}$ at 1.53 V versus RHE, almost 2.0 times higher than that of the Ir/C catalyst (right part of Figure 4b). When the electrolyte was switched to



DOI: 10.1021/acscentsci.8b00426
ACS Cent. Sci. 2018, 4, 1244–1252

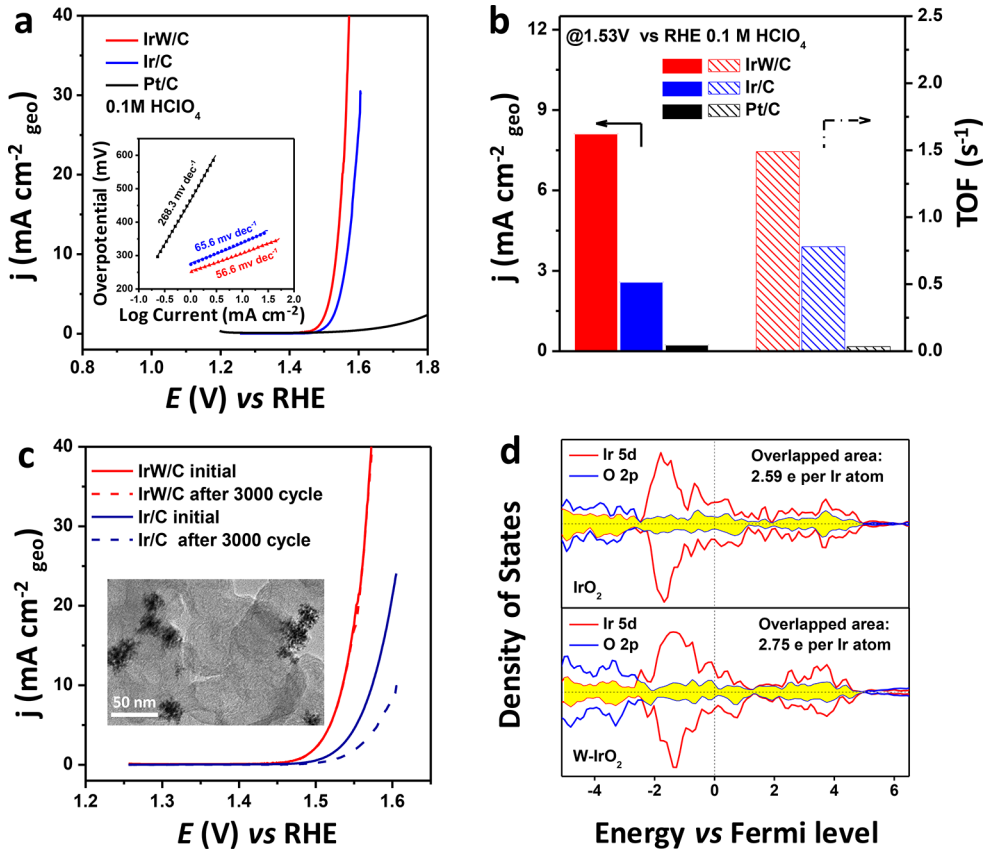


**Figure 4.** OER activity and durability of IrW NDs. (a) OER polarization curves of IrW/C, Ir/C, and Pt/C with 95% *iR*-compensation in 0.1 M $HClO_4$ at the scan rate of 5 mV $s^{-1}$. The inset of part a shows the corresponding Tafel slopes. (b) Current density (left) and TOFs normalized by the ECSA (right) at 1.53 V vs RHE of IrW/C, Ir/C, and Pt/C in 0.1 M $HClO_4$. (c) OER polarization curves of IrW/C and Ir/C before and after a durability test of 3000 cycles between 1.25 and 1.7 V. Inset: TEM image of IrW NDs after a durability test. (d) Projected density of states of $IrO_2$ (up) and W-$IrO_2$ (bottom) with the overlapped states of Ir 5d (red) and O 2p (blue) denoted by the shaded area (yellow).

0.1 M KOH, the IrW/C still shows the lowest Tafel slope of 58.0 mV $dec^{-1}$ and highest TOF of 0.65 $s^{-1}$ among these three catalysts (Figure S18). The results demonstrate that the introduction of W into Ir is able to improve the intrinsic activity of Ir.

The catalytic stability of the OER catalysts remains a critical issue especially in acid electrolyte. We evaluated the durability of the catalysts by cycling the potential between 1.25 and 1.7 V versus RHE for 3000 cycles in 0.1 M $HClO_4$. The IrW/C catalyst shows nearly unchanged polarization curves before and after 3000 cycles, revealing the superb stability. On the contrary, the Ir/C catalyst has a rapid loss of current density, and its positive shift of polarization curves is about 34 mV at 10 mA $cm^{-2}$ (Figure 4c). Furthermore, we investigated the structure and element distribution of the catalyst after a durability test by TEM and EDS mapping. Most Ir nanoparticles in Ir/C were aggregated while the porous structure of IrW NDs was reserved (Figures S19 and S20). The EDS-mapping results reveal that there is almost no change in the atomic ratio of Ir and W (slightly increased from 73.9/26.1 to 75.0/25.0) (Figure S20). Compared with previous reports,[16,17] the W element in IrW catalysts is much more stable than other elements (Fe, Co, Ni, Cu) in Ir-based alloy catalysts. The ICP-AES was also conducted to measure the dissolution amount of iridium ions in the electrolyte after the durability test. As a result, the Ir/C catalyst obviously underwent more severe dissolution of Ir than the IrW/C catalyst (Table S3). X-ray photoelectron spectroscopy (XPS) was performed to understand the chemical state changes of the catalysts before and after the durability test. The Ir 4f spectra of IrW/C and Ir/C indicate that the metallic-state $Ir^0$ was transformed to high-valence $Ir^{4+}$ after the OER durability test (Figure S21). However, the oxidation degree of IrW/C and Ir/C is apparently different, so that the peaks of $Ir^{4+}$ in the spectra of IrW/C are more distinct than those of Ir/C, which means more high-valence Ir(IV) on the surface of the IrW/C catalysts was reserved and did not dissolve in the electrolyte during the long-term durability test. In summary, XPS data, together with ICP-AES and TEM results, indicate that the superb stability of IrW/C results from its aggregation-resistant nanostructure and dissolution-resistant character.

DFT was further implemented to analyze the promoted activity and durability of IrW NDs. Because Ir-based metal catalyst would be usually oxidized to $IrO_2$ in the OER process,[16] rutile $IrO_2$ and W-substituted $IrO_2$ were chosen for approximately modeling the Ir and IrW alloy catalysts after oxidation (Figure S22). The adsorption of oxygen intermediates on the catalyst has important implications for their OER activity. We optimized the geometric structure to evaluate the binding energy of OH, O, and OOH species on the $IrO_2$ and W-substituted $IrO_2$, and the representative optimized geometries are presented in Figure S23. The W-substituted $IrO_2$ has relatively lower binding energy for the oxygen intermediates as compared to $IrO_2$ (Table S4), which is beneficial for approaching the optimal binding energy. Therefore, the enhanced OER activity of IrW/C can be ascribed to the weakened absorption of oxygen intermediates induced by alloying Ir


DOI: 10.1021/acscentsci.8b00426
ACS Cent. Sci. 2018, 4, 1244−1252

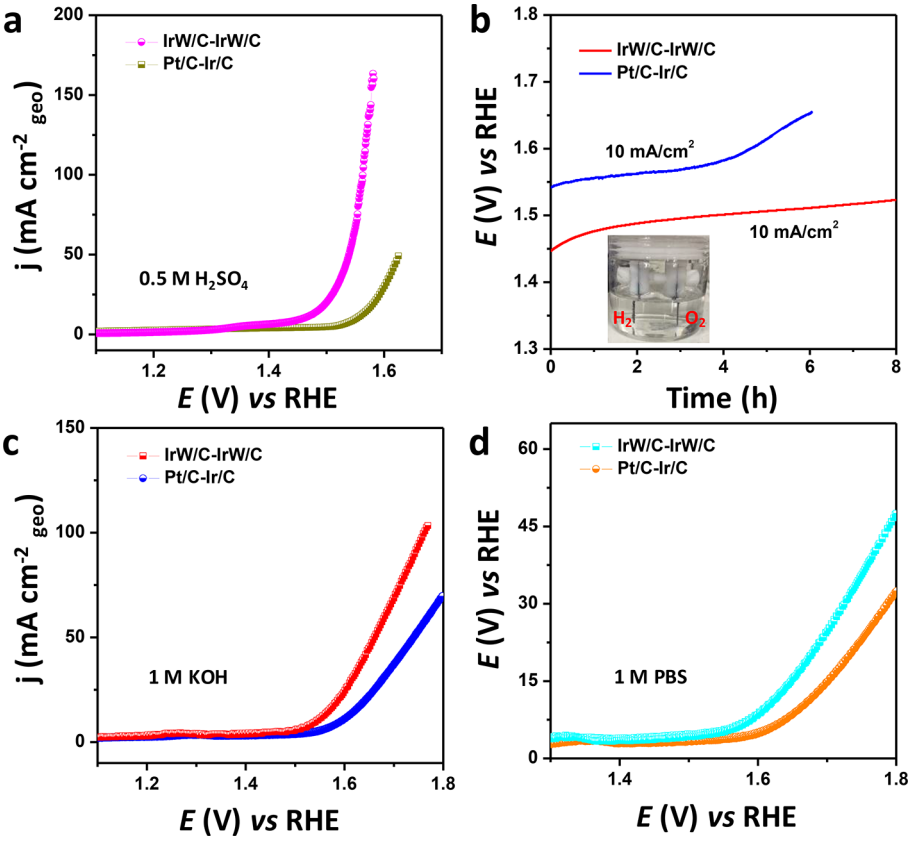


**Figure 5.** Overall water-splitting performance of IrW NDs. (a) Polarization curves of IrW/C−IrW/C and Pt/C−Ir/C for overall water splitting in 0.5 M $H_2SO_4$ at the scan rate of 10 mV $s^{-1}$. (b) Long-term stability tests of IrW/C−IrW/C and Pt/C−Ir/C. Inset: water-splitting device at working conditions. (c, d) Polarization curves of IrW/C−IrW/C and Pt/C−Ir/C for overall water splitting in 0.5 M $H_2SO_4$ and 1 M PBS at the scan rate of 10 mV $s^{-1}$.

with W. Furthermore, the left shift of the Ir 5d d-band center (−1.74 eV for Ir and −1.82 eV for IrW) away from the Fermi level also confirms the weakened adsorption.

To further shed light on the enhanced stability, we calculated the projected density of states of Ir 5d and O 2p orbitals and integrated the overlapped area of the orbitals (Figure 4d). The results show that the overlapped area of W-$IrO_2$ (2.75 $e^-$) is larger than that of $IrO_2$ (2.59 $e^-$). The larger overlapped area of Ir 5d and O 2p orbitals indicates stronger interaction between Ir cations and O anions in the ternary oxide, which improves the dissolution resistance of Ir and stabilizes the catalytic surface. This is consistent with the experimental measurement of fewer dissolved iridium ions in the IrW/C catalyst after the cycling test.

**Overall Water-Splitting Performance.** Inspired by excellent HER and OER performances of the IrW/C catalyst in a three-electrode system, we further assess the activity of IrW NDs as bifunctional catalysts for overall water splitting in a two-electrode electrolyzer. The IrW NDs supported on the carbon fiber paper (CFP) were used for both cathode and anode. The combined system of Pt/C and Ir/C on the CFP (Pt/C−Ir/C) as the cathode and anode was set for comparison. Figure 5a shows the polarization curves of different catalysts in 0.5 M $H_2SO_4$. At the current densities of 10 and 50 mA $cm^{-2}$, only an overpotential of 250 and 310 mV is required for the IrW/C catalyst, much lower than those of Pt/C (320 mV) and Ir/C (390 mV) catalysts. Such activity represents the best level among the state-of-art catalysts reported before (Table S5). More importantly, the IrW/C catalyst also exhibits better durability at a current density of 10 mA $cm^{-2}$ (Figure 5b). The IrW/C catalyst shows a slower increase of the overpotential (from 1.45 to 1.52 V) than the mixed Pt/C and Ir/C catalysts (from 1.55 to 1.67 V) after a long-time chronopotentiometry test.

We also examined the overall water-splitting property of the IrW/C catalyst in alkaline and neutral media by linear voltammetry (Figure 5c,d). In alkaline and neutral media, the IrW/C catalyst presents depressed activity on account of its more sluggish proton transfer than in acid media. However, the IrW/C catalyst still possesses the onset potential of 1.50 V in 1 M KOH and 1.55 V in 1 M phosphate-buffered solution (PBS), lower than those of the Pt/C−Ir/C catalysts in the same media (1.55 and 1.60 V). This implies that the IrW/C catalyst has the potential to catalyze water into $H_2$ and $O_2$ in a wide pH range, which has rarely been reported.

## CONCLUSION

To summarize, we demonstrate a new class of IrW NDs with porous structure as excellent pH-universal bifunctional catalysts for highly efficient overall water-splitting catalysis. We first found that alloying Ir with W is an unrivaled strategy for achieving enhanced bifunctional catalysis for the HER and OER. For the HER, the IrW ND catalyst presents ∼2 times higher HER TOF per Ir site than the commercial Pt/C catalyst in acid and alkaline solution. The DFT calculations reveal that the HER activities in acid and base are linked to the H and OH binding energy optimization by alloying Ir with W, respectively. The IrW NDs also show excellent OER activity,


DOI: 10.1021/acscentsci.8b00426
ACS Cent. Sci. 2018, 4, 1244−1252

which can achieve 8.1 mA $cm^{-2}$ at the overpotential of 300 mV, much higher than that of Ir/C. They also show excellent stability with no activity degradation after 3000 cycles. The theoretical calculation proves that W can stabilize the formed active iridium oxide during the OER process because the doping can induce stronger bonding of Ir and O, hence hindering the dissolution of Ir. Meanwhile, the W-doped $IrO_2$ possesses lower binding energy of oxygen intermediates than $IrO_2$, accelerating its OER kinetics. Because of surface and electronic structure engineering, the superb bifunctional HER and OER performance of IrW NDs can allow their use in a high-performance water electrolyzer at all pH values. The present work provides a new vision for developing new Ir-based alloy catalysts for future renewable energy applications.

## METHODS

**Chemicals.** Iridium chloride hydrate ($IrCl_3 \cdot xH_2O$, 99.8%) was purchased from Alfa Aesar. Hexacarbonyltungsten ($W(CO)_6$, 97%) and oleylamine (OAM, 68−70%) were purchased from Sigma-Aldrich. Cetyltrimethylammonium chloride (CTAC,99%), was purchased from J&K Scientific, Ltd. Glucose ($C_6H_{12}O_6$, 99%), potassium hydroxide (KOH, 95%) and perchloric acid ($HClO_4$, 70−72%) were purchased from Aladdin Reagent Co., Ltd. Commercial Pt/C (20 wt % of 3 nm Pt nanoparticles on carbon black) was purchased from JM Corporation. Commercial Ir/C (20 wt % of 2−4 nm Ir nanoparticles on carbon black) was purchased from Premetek Company. All the chemicals were used without further purification. The water used in all experiments was ultrapure (18.2 MΩ). No unexpected or unusually high safety hazards were encountered.

**Synthesis of IrW NDs.** Iridium chloride hydrate ($IrCl_3 \cdot xH_2O$, 8 mg), tungsten hexacarbonyl ($W(CO)_6$, 10 mg), cetyltrimethylammonium chloride (CTAC, 60 mg), glucose (40 mg), and oleylamine (5 mL) were added into a vial (volume: 20 mL). After the vial had been capped, the mixture was ultrasonicated for around 30 min. The resulting homogeneous clear mixture was then heated in an oil bath at 250 °C for 3 h. The cooled product was washed twice with a cyclohexane/ethanol mixture, and collected by centrifuging at 9500 rpm.

**Characterization.** Transmission electron microscopy (TEM) was conducted on an FEI Tacnai T20 transmission electron microscope at an acceleration voltage of 120 kV. High-resolution TEM (HRTEM) and TEM energy-dispersive X-ray spectroscopy (TEM-EDS) were conducted on a JEM-2100F transmission electron microscope at an acceleration voltage of 200 kV. High-angle annular dark-field scanning TEM (HAADF-STEM) was performed on an FEI TITAN transmission electron microscope at an acceleration voltage of 300 kV. X-ray diffractometry (XRD) was collected on a PANalytical-XRD instrument using a Cu K$\alpha$ radiation ($\lambda$ = 0.154 06 nm) at 40 kV voltage and 30 mA current. X-ray photoelectron spectroscopy (XPS) tests were done with a Kratos AXIS Supra/Ultra spectrometer. The composition and concentration of catalyst were determined by the inductively coupled plasma atomic emission spectroscopy (710-ES, Varian, ICP-AES). The catalysts after the durability tests were scratched off the glassy carbon electrode by sonication in ethanol, and then collected for further TEM characterization.

**Electrochemical Tests.** Before the electrochemical tests, the IrW NDs dispersed in 10 mL of cyclohexane and Ketjen carbon in 50 mL of ethanol were mixed, and then sonicated for 60 min. The obtained IrW/C was collected, washed with ethanol three times, and dried at 80 °C overnight. For the catalyst ink for the electrochemical tests, the carbon-supported catalysts were dispersed in a mixture containing water, isopropanol, and 5 wt % Nafion (volume ratio: 0.5:0.5:0.025) to form a homogeneous ink by sonication for 60 min in an ice bath. The concentration of Ir was controlled to be 0.2 $mg_{Ir}$ $mL^{-1}$ on the basis of the ICP-AES measurement. Electrochemical tests were conducted on a CHI660E electrochemical workstation (Chenhua, Shanghai, China) with a three-electrode system. The catalyst ink modified on a rotating disk glass carbon (GC) electrode (Pine Ins) was used as the working electrode (mass loading: 10.2 $\mu g_{Ir\text{-}or\text{-}Pt}$ $cm^{-2}$), Ag/AgCl (in acid) or Hg/HgO (in base) electrode used as the reference electrode, and a Pt wire (for the OER) or graphite rod electrode (for the HER) used as the counter electrode. The HER and OER electrochemical performances were tested in $N_2$- and $O_2$-saturated acid (0.1 M $HClO_4$) or base (0.1 M KOH) solution. The linear sweep voltammetry curves were recorded with a scan rate of 5 mV $s^{-1}$ and a rotation rate of 2000 rpm (to remove the adsorbed bubbles on the GC) with 95% *iR* drop compensation after the activation or oxidation process of catalysts. The overall water splitting was performed in three electrolytes with different pH values (0.5 M $H_2SO_4$, 1 M KOH, and 1 M PBS) using catalyst ink modified on CFP as both the cathode and anode in a two-electrode system. The active geometric area of both electrodes is 1 cm × 1 cm, and the mass loading is about 30 $\mu g_{Ir\text{-}or\text{-}Pt}$ $cm^{-2}$. Chronopotentiometry (CP) curves were recorded at a constant potential without *iR*-compensation. The electrochemically active surface area (ECSA) was determined by integrating the hydrogen adsorption charge on the CVs at room temperature in $N_2$-saturated 0.1 M $HClO_4$ solution. All the electrochemical data have been tested at least three times. The turnover frequency (TOF) value measured by the ECSA of the catalyst was evaluated at the overpotential of 10 mV (for the HER) and 300 mV (for the OER) versus RHE according to the reported method.[25] The TOF value was calculated from the following equation: $\mathrm{TOF} = \frac{jA}{nFN}$. Here, $j$ is the current density under a certain overpotential with 95% *iR*-corrected, $A$ is the geometric area of the GC electrode (0.196 $cm^{-2}$), $n$ is the number of electron transfer in the reaction (2 for the HER or 4 for the OER), $F$ is the Faraday constant, and $N$ is the mole number of precious metal on the electrode as the active site, calculated by the following equation: $N = \frac{\mathrm{ECSA} \cdot M}{N_0 N_A}$. Here, ECSA is the measured electrochemically active surface area, $M$ is the mass loading of Pt or Ir on the electrode, $N_0$ is the constant of metal surface concentration ($1.25 \times 10^{19}$ $m^{-2}$ for Pt and $1.30 \times 10^{19}$ $m^{-2}$ for Ir), and $N_A$ is the Avogadro constant.

**DFT Calculations.** The computations were implemented by the Vienna ab initio simulation package (VASP) based on density functional theory (DFT) to optimize the structure and investigate the reaction mechanisms. Projector augmented wave (PAW) was used to depict the ion−electron interactions when the function of Perdew, Burke, and Ernzerhof (PBE)[26] based on the generalized gradient approximation (GGA) was adopted to describe the exchange and correlation potential. The Gaussian smearing method with a width of 0.05 eV is used for partial occupancies in finite temperature. In structure optimization calculations, 5 × 5 × 1 Monkhorst−Pack[27] sampled *k*-points were used, and a cutoff energy of 400 eV was adopted. For projected density of states (DOS) plotting, a larger set of *k*-points (17 × 17 × 17) was used. The threshold


DOI: 10.1021/acscentsci.8b00426
ACS Cent. Sci. 2018, 4, 1244−1252

of convergence was set to $1 \times 10^{-4}$ eV and 0.01 eV $Å^{-1}$ for the self-consistent field (SCF) and ion steps, respectively. In all the investigated slab models, the vacuum space is set to be at least 20 Å to separate the interaction between neighboring slabs, with the thickness of more than 10 Å adopted, and all the ions in the slab relaxed. The lattice parameters were optimized at $a = b = 4.52$ Å and $c = 3.16$ Å for rutile $IrO_2$, and $a = b = c = 3.84$ Å for face-centered cubic Ir, consistent with experimental values. Spin polarization was considered in all the computations.

For calculating the free energy diagram of the HER, $\sqrt{3} \times \sqrt{3}$ supercells of (111) facets of the *fcc* Pt, Ir, and IrW model were considered in the computations. We used the method developed by a previous work[28] for the HER in acidic media. For the mechanism in alkaline media, we suppose that it follows the Volmer–Heyrovsky route, in accordance with the experimentally observed Tafel slope.[24] The two stages of hydrogen evolution were as in the follow equations:

$$* + H_2O + e^- = *H + OH^- \text{ (Volmer stage)}$$

$$*H + H_2O + e^- = * + H_2 + OH^- \text{ (Heyrovsky stage)}$$

The corresponding free energy was calculated as follows:

$$\Delta G = \Delta E + \Delta ZPE - T\Delta S - n\Delta G_{OH^- - *OH}$$

where $\Delta E$, $\Delta ZPE$, $T$, and $\Delta S$ are the DFT-derived energy, zero point energy, the temperature in Kelvin, and entropy, respectively. The ZPE (Table S6) was calculated by using vibration frequencies with harmonic normal mode approximation, as in the equation $ZPE = \frac{1}{2}\sum h\nu$, where $h$ is Planck's constant. For the acquisition of $\Delta G_{OH^- - *OH}$, the method of a previously reported work was adopted for avoiding the difficulty in directly calculating the energy of $OH^-$.[29] The barriers of the Volmer stage and Heyrovsky stage are estimated by nudged elastic band (NEB) method.[30]

To simulate the mechanism of OER, we performed the calculations of adsorption energy of OH, O, and OOH over the slab model of the $IrO_2$ (110) surface. For the building of structures of W-$IrO_2$, Ir atoms were homogeneously replaced by W atoms according to the experimentally measured composition. For computing the overlapped area of O 2p and Ir 5d, the integrated section is between −5 and 5 eV versus Fermi level.

## ■ ASSOCIATED CONTENT

### Supporting Information

The Supporting Information is available free of charge on the ACS Publications website at DOI: 10.1021/acscentsci.8b00426.

Additional data and figures including TEM images, size distribution, HRTEM image, FFT pattern, HAADF-STEM image, CVs, TOF vs *E*, polarization curves, Tafel slopes, schematics, EDS-mapping images, and XPS spectra (PDF)

## ■ AUTHOR INFORMATION


### Corresponding Author

*E-mail: guosj@pku.edu.cn.

### ORCID

Shaojun Guo: 0000-0003-4427-6837


### Notes

The authors declare no competing financial interest.

## ■ ACKNOWLEDGMENTS

This work was financially supported by National Natural Science Foundation of China (51671003), National Key Research and Development Program of China (2016YFB0100201), the Open Project Foundation of State Key Laboratory of Chemical Resource Engineering, start-up funding from Peking University, and Young Thousand Talents Program.

## ■ REFERENCES


(1) Chu, S.; Cui, Y.; Liu, N. The path towards sustainable energy. *Nat. Mater.* **2017**, *16*, 16–22.

(2) Roger, I.; Shipman, M. A.; Symes, M. D. Earth-abundant catalysts for electrochemical and photoelectrochemical water splitting. *Nat. Rev. Chem.* **2017**, *1*, 0003.

(3) Tang, T.; Jiang, W. J.; Niu, S.; Liu, N.; Luo, H.; Chen, Y. Y.; et al. Electronic and Morphological Dual Modulation of Cobalt Carbonate Hydroxides by Mn Doping towards Highly Efficient and Stable Bifunctional Electrocatalysts for Overall Water Splitting. *J. Am. Chem. Soc.* **2017**, *139*, 8320–8328.

(4) Jiao, Y.; Zheng, Y.; Jaroniec, M.; Qiao, S. Z. Design of electrocatalysts for oxygen-and hydrogen-involving energy conversion reactions. *Chem. Soc. Rev.* **2015**, *44*, 2060–2086.

(5) Seh, Z. W.; Kibsgaard, J.; Dickens, C. F.; Chorkendorff, I. B.; Nørskov, J. K.; Jaramillo, T. F. Combining theory and experiment in electrocatalysis: Insights into materials design. *Science* **2017**, *355*, eaad4998.

(6) Durst, J.; Siebel, A.; Simon, C.; Hasche, F.; Herranz, J.; Gasteiger, H. A. New insights into the electrochemical hydrogen oxidation and evolution reaction mechanism. *Energy Environ. Sci.* **2014**, *7*, 2255–2260.

(7) Kuttiyiel, K. A.; Sasaki, K.; Chen, W. F.; Su, D.; Adzic, R. R Core–shell, hollow-structured iridium–nickel nitride nanoparticles for the hydrogen evolution reaction. *J. Mater. Chem. A* **2014**, *2*, 591–594.

(8) Durst, J.; Simon, C.; Hasché, F.; Gasteiger, H. A. Hydrogen oxidation and evolution reaction kinetics on carbon supported Pt, Ir, Rh, and Pd electrocatalysts in acidic media. *J. Electrochem. Soc.* **2015**, *162*, F190–F203.

(9) Strmcnik, D.; Uchimura, M.; Wang, C.; Subbaraman, R.; Danilovic, N.; Van Der Vliet, D.; et al. Improving the hydrogen oxidation reaction rate by promotion of hydroxyl adsorption. *Nat. Chem.* **2013**, *5*, 300–306.

(10) Subbaraman, R.; Tripkovic, D.; Strmcnik, D.; Chang, K. C.; Uchimura, M.; Paulikas, A. P.; et al. Enhancing hydrogen evolution activity in water splitting by tailoring $Li^+$-Ni $(OH)_2$-Pt interfaces. *Science* **2011**, *334*, 1256–1260.

(11) Liang, H. W.; Brüller, S.; Dong, R.; Zhang, J.; Feng, X.; Müllen, K. Molecular metal–$N_x$ centres in porous carbon for electrocatalytic hydrogen evolution. *Nat. Commun.* **2015**, *6*, 7992.

(12) Strmcnik, D.; Lopes, P. P.; Genorio, B.; Stamenkovic, V. R.; Markovic, N. M. Design principles for hydrogen evolution reaction catalyst materials. *Nano Energy* **2016**, *29*, 29–36.

(13) Seitz, L. C.; Dickens, C. F.; Nishio, K.; Hikita, Y.; Montoya, J.; Doyle, A.; et al. A highly active and stable $IrO_x/SrIrO_3$ catalyst for the oxygen evolution reaction. *Science* **2016**, *353*, 1011–1014.

(14) Reier, T.; Nong, H. N.; Teschner, D.; Schlögl, R.; Strasser, P. Electrocatalytic Oxygen Evolution Reaction in Acidic Environments-Reaction Mechanisms and Catalysts. *Adv. Energy Mater.* **2017**, *7*, 1601275.

(15) Reier, T.; Pawolek, Z.; Cherevko, S.; Bruns, M.; Jones, T.; Teschner, D.; et al. Molecular Insight in Structure and Activity of Highly Efficient, Low-Ir Ir-Ni Oxide Catalysts for Electrochemical Water Splitting (OER). *J. Am. Chem. Soc.* **2015**, *137*, 13031–13040.

(16) Park, J.; Sa, Y. J.; Baik, H.; Kwon, T.; Joo, S. H.; Lee, K. Iridium-Based Multimetallic Nanoframe@Nanoframe Structure: An Efficient and Robust Electrocatalyst toward Oxygen Evolution Reaction. *ACS Nano* **2017**, *11*, 5500–5509.




DOI: 10.1021/acscentsci.8b00426
*ACS Cent. Sci.* 2018, 4, 1244–1252

(17) Pi, Y.; Shao, Q.; Wang, P.; Guo, J.; Huang, X. General formation of monodisperse IrM (M= Ni, Co, Fe) bimetallic nanoclusters as bifunctional electrocatalysts for acidic overall water splitting. *Adv. Funct. Mater.* **2017**, *27*, 1700886.
(18) Pfeifer, V.; Jones, T. E.; Vélez, J. J. V.; Arrigo, R.; Piccinin, S.; Hävecker, M.; et al. In situ observation of reactive oxygen species forming on oxygen-evolving iridium surfaces. *Chem. Sci.* **2017**, *8*, 2143−2149.
(19) Man, I. C.; Su, H. Y.; Calle - Vallejo, F.; Hansen, H. A.; Martínez, J. I.; Inoglu, N. G.; et al. Universality in oxygen evolution electrocatalysis on oxide surfaces. *ChemCatChem* **2011**, *3*, 1159−1165.
(20) Feng, J.; Lv, F.; Zhang, W.; Li, P.; Wang, K.; Yang, C.; Wang, G. C.; et al. Iridium-Based Multimetallic Porous Hollow Nanocrystals for Efficient Overall-Water-Splitting Catalysis. *Adv. Mater.* **2017**, *29*, 1703798.
(21) Jovanovic, P.; Hodnik, N.; Ruiz-Zepeda, F.; Arcon, I.; Jozinovic, B.; Zorko, M.; et al. Electrochemical Dissolution of Iridium and Iridium Oxide Particles in Acidic Media: Transmission Electron Microscopy, Electrochemical Flow Cell Coupled to Inductively Coupled Plasma Mass Spectrometry, and X-ray Absorption Spectroscopy Study. *J. Am. Chem. Soc.* **2017**, *139*, 12837−12846.
(22) Cherevko, S.; Geiger, S.; Kasian, O.; Kulyk, N.; Grote, J. P.; Savan, A.; et al. Oxygen and hydrogen evolution reactions on Ru, $RuO_2$, Ir, and $IrO_2$ thin film electrodes in acidic and alkaline electrolytes: a comparative study on activity and stability. *Catal. Today* **2016**, *262*, 170−180.
(23) Kim, Y. T.; Lopes, P. P.; Park, S. A.; Lee, A. Y.; Lim, J.; Lee, H.; et al. Balancing activity, stability and conductivity of nanoporous core-shell iridium/iridium oxide oxygen evolution catalysts. *Nat. Commun.* **2017**, *8*, 1449.
(24) Conway, B.; Tilak, B. Interfacial processes involving electrocatalytic evolution and oxidation of $H_2$, and the role of chemisorbed H. *Electrochim. Acta* **2002**, *47*, 3571−3594.
(25) Zhang, B.; Zheng, X.; Voznyy, O.; Comin, R.; Bajdich, M.; García-Melchor, M.; et al. Homogeneously dispersed multimetal oxygen-evolving catalysts. *Science* **2016**, *352*, 333−337.
(26) Perdew, J. P.; Burke, K.; Ernzerhof, M. Generalized gradient approximation made simple. *Phys. Rev. Lett.* **1996**, *77*, 3865.
(27) Monkhorst, H. J.; Pack, J. D. Special points for Brillouin-zone integrations. *Phys. Rev. B* **1976**, *13*, 5188.
(28) Nørskov, J. K.; Bligaard, T.; Logadottir, A.; Kitchin, J. R.; Chen, J. G.; Pandelov, S.; Stimming, U. Trends in the exchange current for hydrogen evolution. *J. Electrochem. Soc.* **2005**, *152*, J23−J26.
(29) Nørskov, J. K.; Rossmeisl, J.; Logadottir, A.; Lindqvist, L. R. K. J.; Kitchin, J. R.; Bligaard, T.; Jonsson, H. Origin of the overpotential for oxygen reduction at a fuel-cell cathode. *J. Phys. Chem. B* **2004**, *108*, 17886−17892.
(30) Henkelman, G.; Uberuaga, B. P.; Jónsson, H. A climbing image nudged elastic band method for finding saddle points and minimum energy paths. *J. Chem. Phys.* **2000**, *113*, 9901−9904.



DOI: 10.1021/acscentsci.8b00426
*ACS Cent. Sci.* 2018, 4, 1244−1252